nature photonics

ARTICLES

https://doi.org/10.1038/s41566-022-00995-z

Single-pass high-efficiency terahertz free-electron laser

A. Fisher[1]✉, Y. Park[1]✉, M. Lenz[1], A. Ody[1], R. Agustsson[2], T. Hodgetts[2], A. Murokh[2] and P. Musumeci[1]✉

The terahertz gap is a region of the electromagnetic spectrum where high average and peak power radiation sources are scarce while at the same time scientific and industrial applications are growing in demand. Free-electron laser (FEL) coupling in a magnetic undulator is one of the best options for radiation generation in this frequency range, but slippage effects require the use of relatively long and low-current electron bunches to drive the terahertz FEL, limiting amplification gain and output peak power. Here we use a circular waveguide in a 0.96-m strongly tapered helical undulator to match the radiation and electron-beam velocities, allowing resonant energy extraction from an ultrashort 200-pC 5.5-MeV electron beam over an extended distance. Electron-beam spectrum measurements, supported by energy and spectral measurement of the terahertz FEL radiation, indicate an average energy efficiency of ~10%, with some particles losing >20% of their initial kinetic energy.

Compact and efficient high average and peak power terahertz radiation sources are highly desired for many scientific and industrial applications, including time-domain spectroscopy, high-field resonant and non-resonant excitation of solid-state systems, fusion research and high-gradient acceleration, and terahertz-based imaging for medical and security applications[1–6]. Among the various sources of electromagnetic power in the 0.1–10 THz frequency range, free-electron lasers (FELs), based on the ponderomotive interaction between an electromagnetic wave and a relativistic electron beam co-propagating in a magnetic undulator, are particularly attractive due to the scarcity of high-power solid-state sources and because the required electron beam and undulator parameters are readily achievable with current technology[7,8]. Other vacuum electronics devices,such as klystrons, travelling-wave tubes and backward-wave oscillators, which are the workhorses in the microwave regime (0.1–100 GHz) have reduced output at higher frequencies due to the limitations associated with the wavelength-scale transverse apertures of the slow wave structures[9]. Fast-wave coupling schemes (like gyrotrons) extend well into the sub-terahertz frequency range (up to a few hundred gigahertz) and can reach relatively higher power and efficiencies in the tens of percent[10,11], but are based on the use of non (or mildly) relativistic electron beams, reducing the frequency scalability and limiting the maximum peak power available. In addition, FELs have unique advantages, including frequency tunability, high peak power and repetition rates only limited by electron-beam availability. Many FEL facilities have played important roles in the development of terahertz science[12–17], with more user facilities coming online[18–20] and even more planned for future years[21–23].

At the same time, the FEL interaction presents some characteristic challenges in the long-wavelength regime as single-pass gain in the undulator is typically limited due to slippage and diffraction effects. The majority of the FELs listed above operate using long (many wavelengths) electron bunches with relatively low peak current densities and use a resonator configuration to build up power in an optical cavity. Advances in high-brightness (that is, high peak current, low transverse emittance) electron-beam sources[24] enable the generation of ultrafast electron bunches with very high current densities and strong coupling to the radiation. On the other hand, due to the different velocities of beam and radiation in the undulator (slippage), shortening the electron bunch quickly leads to a temporal walk-off between the field and current profiles along the interaction, which is detrimental to efficient energy extraction.

In this Article we combine two different concepts in FEL physics to overcome these challenges and show extremely high (~10%) conversion efficiency in a single pass through the undulator. First, we leverage our recent experimental results on the use of a waveguide to enhance ponderomotive FEL coupling at long wavelengths[25,26]. The immediate advantage of using the waveguide is to transversely confine the radiation, limiting the effects of diffraction, which, at long wavelengths, would severely degrade the interaction. Another critical added benefit is that, by properly choosing the waveguide radius, it is possible to match the group velocity of the fundamental resonant mode of the waveguide to the average longitudinal velocity of the electron beam in the undulator. When the interaction is tuned to this so-called zero-slippage condition (Fig. 1a), the electromagnetic radiation envelope, instead of slipping forward by one wavelength each undulator period (as in a regular FEL), remains temporally aligned with a short electron beam during the entire interaction[27–29]. This situation is very advantageous for a terahertz FEL, as strong coupling with high-current compressed electron beams can now occur over much longer interaction lengths. In the frequency domain, as shown in Fig. 1b, the bandwidth of the waveguide FEL interaction at the grazing resonance (red shaded region) is much larger than the typical FEL bandwidth (red dashed line) for the free-space case, supporting the amplification of shorter radiation pulses.

The other key element we add to maximize the energy extraction of this configuration is the strong tapering of the undulator to enhance stimulated superradiant radiation emission (TESSA) from the injected electron bunch[30–32]. In a constant-parameter (untapered) FEL, the interaction length would otherwise be limited by gain saturation, which occurs when the electrons lose enough energy to the radiation to drop out of resonance. By adjusting the

[1]UCLA Department of Physics and Astronomy, Los Angeles, CA, USA. [2]RadiaBeam Technologies, Santa Monica, CA, USA. ✉e-mail: afisher000@g.ucla.edu; ypark@physics.ucla.edu; musumeci@physics.ucla.edu

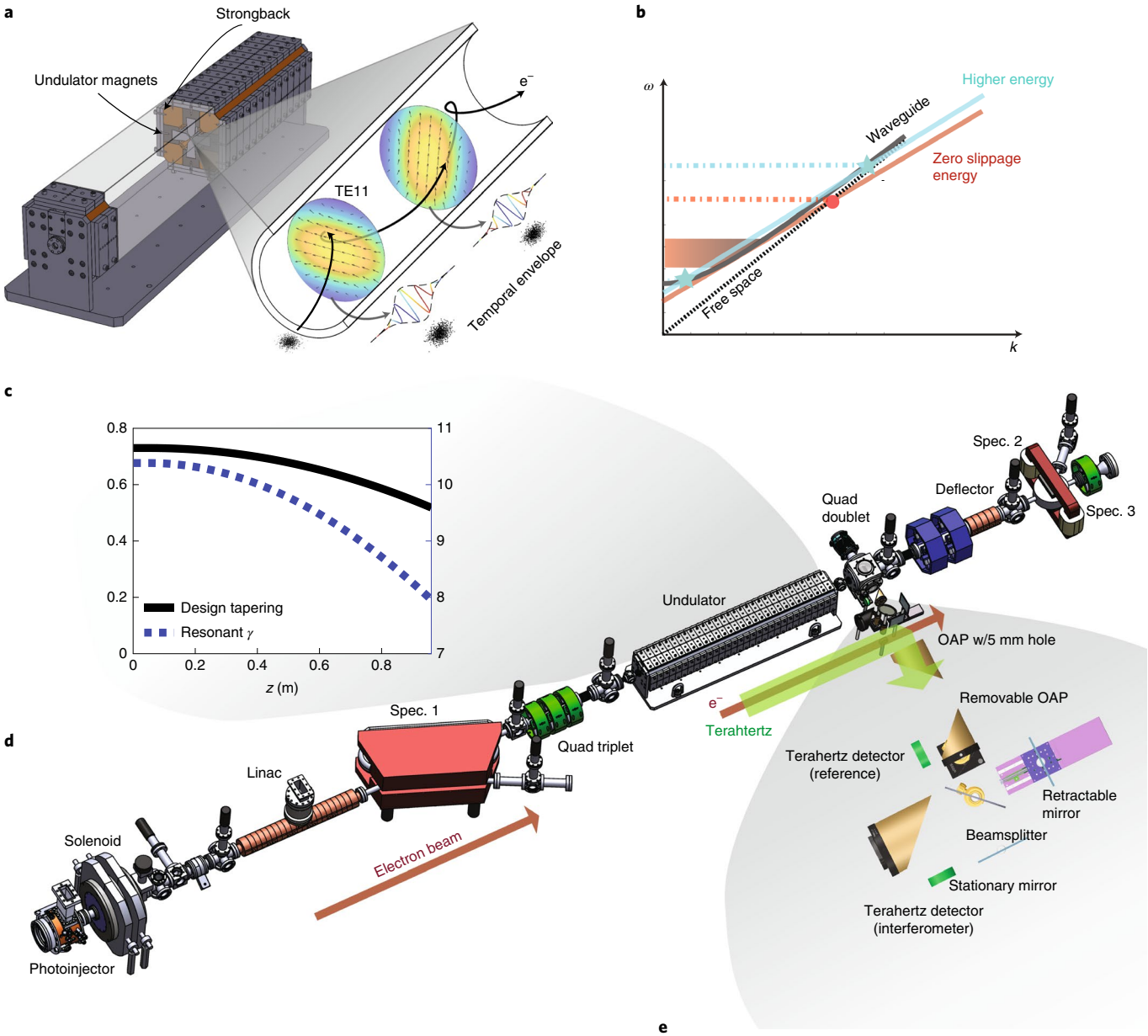

Fig. 1 | Tapering-enhanced zero-slippage terahertz FEL scheme. a, Cartoon of the zero-slippage FEL interaction between relativistic electrons and the TE11 mode of a circular waveguide in a helical undulator. **b**, Dispersion diagram for a waveguide FEL. Resonant phase matching occurs when the phase velocity of the electrons in the undulator (red line) intersects the radiation dispersion curves (black solid for waveguide, dotted for free space). When the two curves have a tangent intersection, the interaction bandwidth (indicated by the shaded red area) is substantially larger than in the free space case (dash-dotted red line, intersection point marked by the red dot). If the e-beam energy is increased (blue solid line), there will be two intersection points (marked by the blue stars) with the waveguide dispersion relation representing the two frequencies branches (blue dash-dotted lines) discussed in the paper below. **c**, Undulator magnetic field amplitude and resonant energy tapering along the undulator. **d**, Pegasus beamline technical drawing showing the photoinjector, the buncher linac, the undulator and the electron-beam diagnostics. **e**, Details of the terahertz diagnostics set-up for pulse energy and interferometry measurements.

magnetic field along the undulator, it is possible to prolong the interaction beyond this limit (Fig. 1c) enabling the demonstration in a single-pass FEL of extremely high efficiencies >10% for the conversion of the electron-beam energy into terahertz pulse energy.

Results

The experiment was carried out at the UCLA Pegasus photoinjector laboratory[33,34], where a 40-fs laser pulse was used to illuminate a Cu photocathode in an S-band radiofrequency (RF) gun to generate up to 200 pC of beam charge (Fig. 1d). The booster linac cavity was tuned in amplitude and phase to deliver at the entrance of a permanent-magnet-based helical undulator (twenty-eight 3.2-cm-long periods and an initial field amplitude 0.73 T) a compressed beam of 5.5 MeV total energy (relativistic γ factor = 11) with a root-mean-square (r.m.s.) bunch length of <1.5 ps. Considering the interaction with the TE11 mode of the 4.54-mm-diameter circular waveguide, which also served as a vacuum pipe in the undulator, we calculated a zero-slippage FEL resonant frequency of 160 GHz.

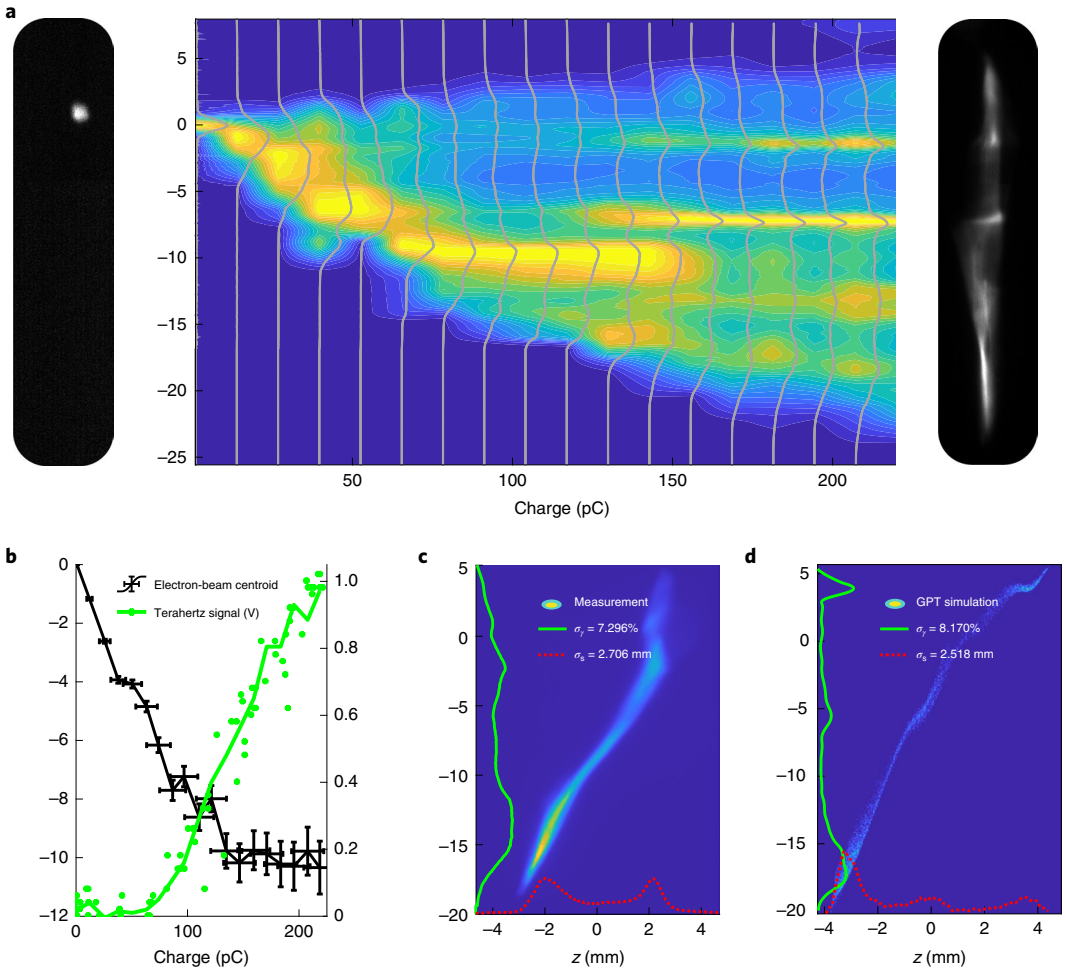

Fig. 2 | Electron beam and THz energy measurements. a, High-resolution electron-beam spectra as a function of the charge injected into the undulator. Two reference raw spectrometer images for the lowest (left) and highest (right) charge are also shown. **b**, Relative beam energy centroid variation and terahertz pulse energy from the reference pyrodetector corresponding to **a**. The horizontal error bars correspond to the width of the charge bins, which is chosen to be equal to the r.m.s. charge fluctuations. The vertical errors on the centroid data represent the r.m.s. of the beam centroid distribution calculated over ≥10 images. **c**,**d**, Measured (**c**) and simulated (**d**) longitudinal phase spaces for a 150-pC injected beam charge. For this comparison, the longitudinal phase space at the exit of the undulator is propagated up to the deflector plane located 6.5 m from the cathode.

The undulator was parabolically tapered by adjusting the gap, starting 5 cm from the entrance, to maintain resonance with an electron beam decelerating by 15% at the end of the 0.96-m undulator length.

The FEL interaction was established by recording the energy profiles of the beam from the high-resolution magnetic spectrometer as well as the terahertz radiation energy measured by the reference pyrodetector (Methods) as a function of the input beam charge. In the contour plot in Fig. 2a, the energy spectra are normalized to better highlight the evolution of the energy distribution as the terahertz FEL interaction grows in strength. For charges above 50 pC, in conjunction with the appearance of a clear signal on the pyrodetector (Fig. 2b), the electron-beam spectrum broadens and redshifts to a lower mean beam energy. The spectra also develop large and deep modulations that are characteristic signatures of the FEL longitudinal phase space dynamics occurring in the tapered undulator[32]. At the highest injected beam charge (220 pC), the average beam energy decreases by 10%, with some particles losing more than 20% of their initial kinetic energy. Taking into account the terahertz pyroelectric detector calibration (145 kV J^{-1}) and the losses in the terahertz transport line, mostly due to apertures and diffraction (73%), the maximum signal recorded on the detector yields an estimated terahertz energy at the undulator exit of 50 μJ, which is in good agreement with the average energy loss by the electron beam, considering the stainless-steel waveguide losses and that only 40% of the injected charge is transmitted through the undulator.

The terahertz signal and the associated electron spectra are well correlated with the injected charge through the undulator (Fig. 2b), with output fluctuations of less than 10% for a given input charge, mostly attributable to energy and pointing fluctuations. The overall stability is remarkable for a single-pass FEL in the absence of an external radiation seed signal, and is explained by the initial bunching from the compressed electron beam, which effectively works as a FEL seeding signal.

The X-band deflector located after the undulator can be used to streak the beam vertically and visualize the longitudinal phase space on the spectrometer screen. A sample phase space corresponding to 150-pC injected charge is shown in Fig. 2d. Although the resolution of the longitudinal phase space measurement is blurred from the large transverse size of the beam in the deflector and relatively large emittance of the beam after the undulator, the most salient features in the beam distribution, such as chirp, energy spread and bunch length, are well reproduced in the measured image. A single decelerating bucket can be identified, in good agreement with the simulation results.

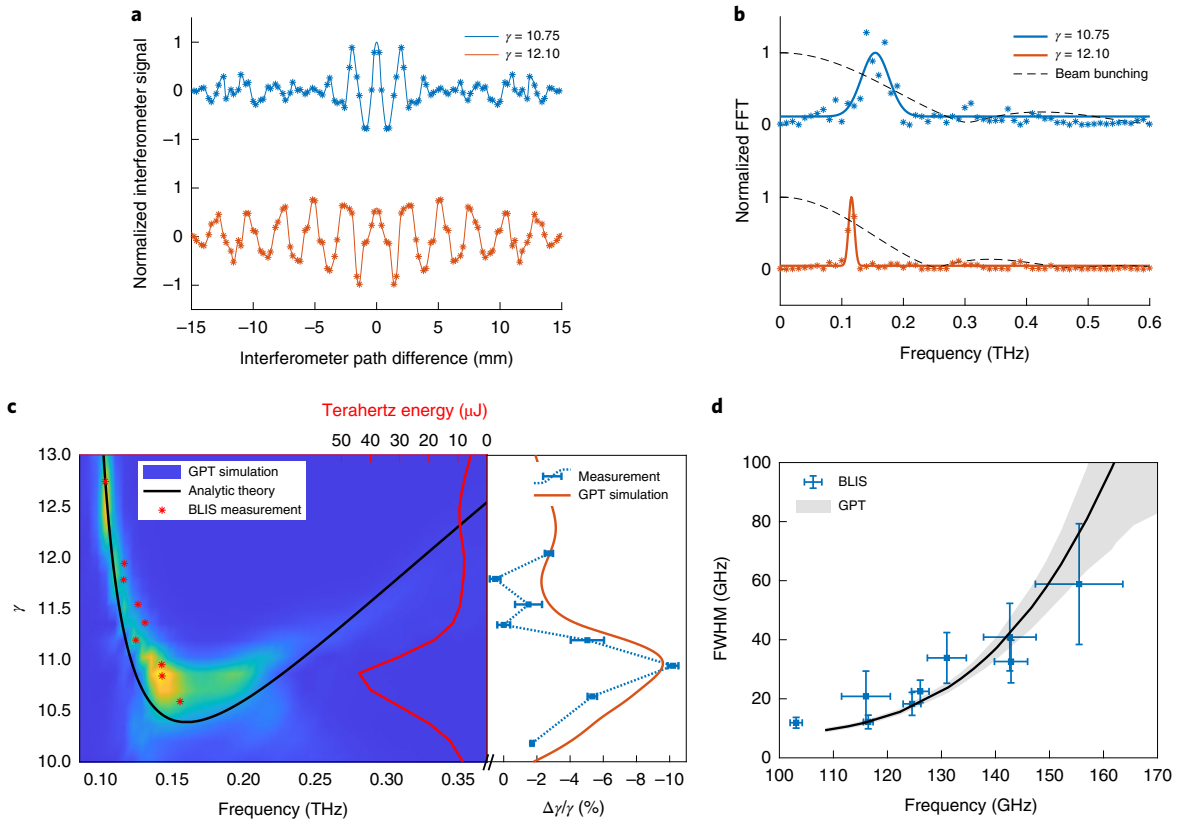

Fig. 3 | Interferometry measurements. a, Interferometer traces for input beam energies near (blue) and above (orange) the zero-slippage condition. **b**, Power spectrum of the emitted radiation, computed from a fast Fourier transform (FFT) of the interferometer traces and plotted together with the beam bunching factors obtained from beam dynamics simulations. **c**, The interferometer peak frequency measurements are compared to general particle tracer (GPT) simulations and to the theoretical phase-resonance curves. The simulated pulse energies show a maximum interaction at a slight positive energy detuning. Measurements of FEL efficiency versus input electron-beam energy are plotted against GPT results. The error bars in the energy loss data represent the r.m.s. of the distribution calculated over ≥10 images. The charge in these simulations is scaled by the observed transmission through the undulator. **d**, Terahertz spectrum bandwidth (FWHM) shown as a function of the peak radiation wavelength for measurements and simulation. Errors bars represent 95% confidence intervals of Gaussian fits to the spectral peaks, like those shown in **b**.

The resonant nature of the interaction was then studied by adjusting the linac phase to vary the initial beam energy and measuring the spectral content using a Michelson interferometer (Fig. 3). Two sample autocorrelation traces and the associated Fourier transforms are displayed for beam energies near (blue) and above (orange) the expected zero-slippage resonant value. Clear differences in period and radiation pulse length can be observed. A more complete scan of the peak frequency and spectral bandwidth is reported in Fig. 3c,d. Notably, the peak frequency is observed to decrease when increasing the beam energy, in a peculiar behaviour for FEL physics, which is well reproduced by the simulations and is discussed in the next section. In Fig. 3d the spectrum full-width at half-maximum (FWHM) is plotted versus the peak frequency. When approaching the zero-slippage condition at 160 GHz, the radiation pulse is only a few cycles long and its relative bandwidth approaches 50%. This occurs for an injection normalized energy $\gamma = 11$, where the largest amount of terahertz energy is predicted and the largest relative deceleration in the electron-beam spectrum is measured.

To complete the description of the experiment, it is important to clarify that all the charge values reported in this Article refer to measurements before the undulator. On the other hand, the transmission through the undulator and through the 5-mm hole in the off-axis parabolic (OAP) mirror located 15 cm after the undulator used to collect and redirect the terahertz radiation was found to be strongly energy-dependent, monotonically decreasing from full transmission at high injection energies to below 40% for lower energies. There are two main reasons for these severe transport losses in the beamline. First, the radius of the helical trajectory r_{max} inside the undulator increases at lower beam energy, reducing the clearance through the small beam pipe. At $\gamma = 10.5$, we have $r_{max} = 1.1$ mm. This also causes the ratio of the trajectory radius to the magnet gap (7 mm) to be extreme and very unusual, with the particles sampling far off-axis fields as they propagate in the undulator. At these large offsets, the undulator field quality cannot be precisely tuned using the conventional methods (Hall probe or pulse wire[35,36]) that are typically used to correct the trajectory assuming small deviations from the undulator axis. Finally, for the lower injected beam energies, the strong natural focusing of the helical undulator implies matched beta functions, which are not practically attainable on the Pegasus beamline, given the upstream limitations in beam transport clearances and the 1.2-m quadrupole/undulator separation. This leads to large betatron oscillations in the undulator (Fig. 4a), which further contribute to the increasing charge losses.

Discussion

To understand these results it helps to recall that the zero-slippage FEL interaction in a waveguide requires tuning of the interaction parameters to satisfy the traditional FEL phase-resonance condition, $(k_z + k_u) = \frac{\omega}{\beta_z c}$, and the group-velocity matching or zero-slippage

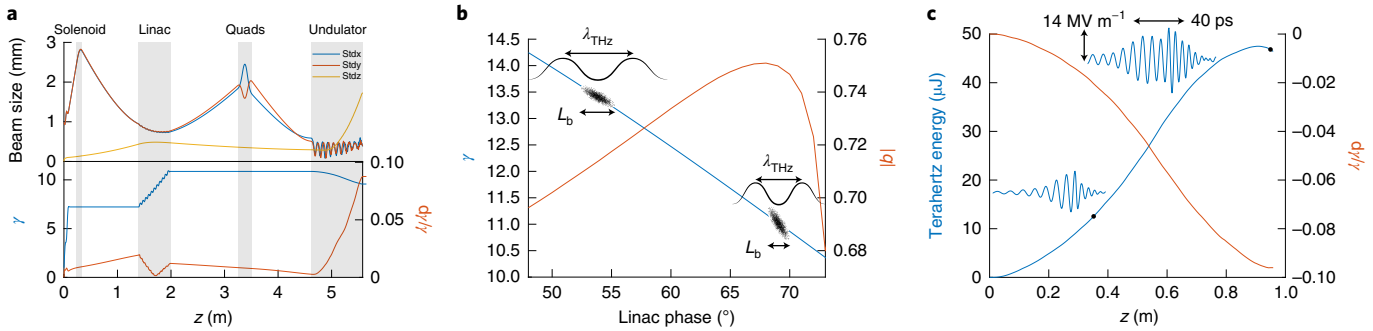

Fig. 4 | THz FEL simulations. a, Beam sizes, energy γ and energy spread $d\gamma/\gamma$ along the Pegasus beamline. **b**, Energy γ and bunching factor $|q|$ for different linac phases. Even though beam compression changes with linac phase, the resonant frequency changes similarly, such that the bunching factor is relatively constant. **c**, Evolution of the terahertz pulse energy and extraction efficiency for a 150-pC injected beam charge and 20% charge transmission through the undulator. Insets: the terahertz pulse along the undulator.

condition, $\frac{c^2 k_z}{\omega} = \beta_z c$. In these expressions, the longitudinal wavenumber k_z and the radiation frequency ω are connected by the waveguide dispersion relation, $\omega^2/c^2 = k_z^2 + k_\perp^2$, where $k_\perp = 1.8412/R$ for the TE11 circular waveguide mode[37], R is the waveguide radius, $k_u = 2\pi/\lambda_u$ where λ_u is the undulator period, and $c\beta_z$ is the beam longitudinal velocity in the undulator. Using $\gamma_{z0} = \gamma_0/\sqrt{1+K^2}$, one can show that the resonant frequency at zero-slippage or grazing resonance is satisfied for $2\pi f_{zs} = ck_u\beta_{z0}\gamma_{z0}^2$, which is one-half the resonant frequency of an FEL in free space and in the relativistic approximation $\gamma_0 = \frac{k_\perp}{k_u}\sqrt{1+K^2}$, where K is the undulator normalized vector potential. The latter of these implies that, for a given waveguide and undulator magnet, there is only one beam energy for which both group-velocity and phase-velocity matching can be achieved at the same time. It also follows from these relations that the ratio of the helical beam trajectory radius r_{max} to the waveguide radius R is $\frac{r_{max}}{R} = \frac{1}{1.8412}\frac{K}{\sqrt{1+K^2}} \leq 0.543$, which helps to quantify the challenges in obtaining full charge transmission through the undulator.

Figure 3c plots the theoretical phase-resonance condition, which can be simply obtained as the intersection between the electron beam and waveguide dispersion curves as shown in Fig. 1b. At $\gamma = \gamma_0$, there is exactly one solution and the zero-slippage condition is satisfied. For $\gamma < \gamma_0$, there are no solutions to the phase-resonance condition. For a beam energy larger than the grazing incidence condition ($\gamma > \gamma_0$), interaction can occur at two resonant frequencies where the waves will be group-velocity mismatched with the electron beam with the higher (lower) frequency moving faster (slower) than the beam. An approximation of the phase-resonant frequencies for relativistic beams ($\beta_z \approx 1$) is $f = f_{zs}\left(1 + \frac{2\Delta\gamma}{\gamma_0}\right)\left(1 \pm \sqrt{\frac{2\Delta\gamma}{\gamma_0}}\right)$, where $\Delta\gamma = \gamma - \gamma_0$. In Fig. 3c, the measured peak frequencies at different input beam energies are overlaid and found to closely follow the lower frequency branch of the analytical curve.

A better comparison is obtained using a numerical simulation of the interaction based on a GPT extension module[38] that self-consistently calculates the interaction of the electromagnetic field and electrons inside the undulator and takes into account both dispersion and three-dimensional (3D) space charge effects. The measurements and the simulations both predict that the largest terahertz pulse energy is produced from beams slightly detuned from the analytical zero-slippage condition. This is due to the beam energy spread and transverse emittance, which contribute to a finite bandwidth for the electron-beam dispersion line. Electrons having energies below the zero-slippage resonant condition cannot be phase-matched with the electromagnetic field, so a higher injection mean energy maximizes the number of particles participating to the interaction. Losses from ohmic heating of the waveguide are also included in the simulation model using the calculated frequency-dependent attenuation constant (~3.5 dB m^{-1} at 160 GHz) for the TE11 mode in a stainless-steel waveguide and they were found to reduce the terahertz energy by 37% compared to the infinite conductivity case. It is worthwhile pointing out that the Pegasus beam dynamics simulations are also performed with GPT, so this is the first FEL experiment entirely simulated (start-to-end) within a single code[39].

The seed for the FEL amplification is provided by the initial bunching of the electron beam. In other words, when the compressed beam enters the undulator (Fig. 4a), superradiant emission of the radiation will occur as the bunch length is comparable to the radiation wavelength[40]. The radiation is then slowed down by the waveguide and interacts back with the beam, continuing to decelerate it along the undulator. Owing to the fact that the longer wavelengths are going to be more strongly excited by the electron-beam spectrum (Fig. 3b), the lower-frequency branch is favoured in the interaction. For this reason, as we tune the electron-beam energy higher, the FEL radiation redshifts instead of the more natural quadratic blueshift seen in many other FEL set-ups.

It is also important to observe that as the linac RF phase is tuned off crest, the beam energy changes, but the bunching factor at the resonant frequency remains nearly constant at ~0.7. In fact, for phases closer to the crest of the RF accelerating wave (chosen as the reference zero point on the horizontal axis in Fig. 4b), the beam features higher energies, a larger residual chirp and a longer bunch length at the entrance of the undulator, but the resonant wavelength is also longer so that the bunching factor is comparable with what is obtained at much higher compression phases.

It is finally instructive to observe the simulated evolution of the electron-beam and terahertz energy for the zero-slippage parameter case shown in Fig. 4c to illustrate the growth of the signal along the undulator. The behaviour is initially quadratic, matching well the expected tapering curve. Further into the undulator, trapped charge losses as well as dispersive effects limit the energy exchange as the field amplitude reaches nearly 15 MV m^{-1} in the waveguide. The insets show two different snapshots of the longitudinal profile of the electric field along the undulator exhibiting the strong chirp characteristic of a large-bandwidth pulse propagating in a waveguide.

Looking towards the future, by adjusting the beam energy and choosing different waveguide dimensions it will be possible to extend this scheme to the generation of higher frequencies. For example, a 2.9-mm-diameter pipe and an 8-MeV beam satisfy the zero-slippage condition at 0.4-THz resonant FEL frequency. At even higher frequencies (above 1 THz), it becomes increasingly difficult to compress the input electron beam to a bunch length shorter than

the radiation wavelength. In this case, an interesting option to seed the interaction is to use longitudinal beam-shaping techniques to generate a microbunch train at terahertz frequency[41–44]. Injecting a high-peak-current beam that can coherently emit radiation within the FEL acceptance bandwidth is important so as to reach, in a short distance, a sufficiently high electromagnetic intensity to enter the nonlinear regime where the strong tapering facilitates significant energy extraction.

It is useful to review the scaling laws to better understand how the system will perform when a higher beam energy is used to target a higher resonant frequency ($\propto\gamma^2$ when keeping the undulator parameters fixed). Remarkably, the helical trajectory radius r_{max} and the waveguide size R are both inversely proportional to the beam energy, but their ratio remains constant. At the same time, the undulator focusing betatron function increases with beam energy, offsetting the decrease in geometric emittance to keep the matched beam size constant. Assuming a normalized transverse emittance of 2 μm, and the availability of suitable electron optics to inject the beam into the undulator at its matched beam size of <100 μm, it will be possible to scale the beam energy up by one order of magnitude and hence the frequency up by a factor of 100 before significant beam losses are encountered due to transverse motion of the electrons in the pipe. There is also another important consequence of the reduction of the waveguide radius at higher frequencies. As the driving term in the FEL wave equation is proportional to the effective current density (that is, the peak current over the resonant mode cross-section), at higher frequencies a lower beam charge in a shorter bunch length would be sufficient to sustain large electric field amplitudes and achieve similar conversion efficiencies. The total radiation power would be reduced, though, due to the smaller mode area. For example, in the case study mentioned above tuned at 0.4 THz, simulations indicate that, when using a 60-pC beam charge, we can still obtain 40 μJ of terahertz energy with a relatively high conversion efficiency of 8%.

Although the helical geometry features important advantages such as stronger FEL coupling and a circularly polarized output radiation, a planar undulator geometry and adjustable-gap curved parallel-plate waveguide would allow us to tune the zero-slippage resonant condition and obtain high efficiency over a larger frequency range. Wakefield effects in the terahertz waveguide will eventually limit the smallest radius (and therefore the highest frequency) achievable with this scheme. The influence that higher-order modes can have on the transport through the undulator remains to be investigated in detail. In terms of efficiency, larger peak currents and/or longer interaction lengths could be used to maximize the energy conversion. In the present experiment, for example, using a higher beam charge would be beneficial provided that the transmission losses through the undulator could be minimized. It is worthwhile to note, however, that even assuming very large input charges, the efficiency would be limited by the fixed undulator tapering profile, which for this experiment was set at <25% (see the resonant energy profile along the undulator in Fig. 1). Achieving higher efficiency would require re-tuning of the undulator magnetic field profile for the higher beam charge/current input beam. For high-repetition-rate electron sources, an interesting option is to recirculate a fraction of the terahertz radiation and use it as a high-intensity external seed to jumpstart the interaction, improve the capture efficiency and maximize the final terahertz energy. The temporal separation of the electron bunches would have to be matched to the roundtrip of the terahertz cavity, typically on the order of 10–20 ns for an undulator length of 1 m (ref. [45]).

In conclusion, these results pave the way towards very high average and peak power terahertz radiation sources. We demonstrate how the use of the waveguide is critical to counteract two important drawbacks of long-wavelength FELs—diffraction and slippage—thus allowing us to fully reap the benefits of high-brightness beams from photoinjectors and strong undulator tapering. To put the experiment in perspective, the efficiency record in an FEL at 35 GHz (34%) was obtained using 30-ns-long electron pulses from an induction linac in a 3-m-long undulator[46]. Here we show 10% efficiency at 160 GHz in less than 1 m using a beam of a few picoseconds. Compact high-efficiency single-pass terahertz FELs will unlock the potential to reach extremely high fields in a high-demand region of the electromagnetic spectrum, opening entirely new opportunities for terahertz science. From the FEL point of view, this experiment provides a demonstration of the TESSA concept in the high-gain regime, where strong seeding and optimized tapering lead to significant energy extraction from the beam, concurrently with a large radiation power growth along the undulator, therefore constituting an important step forward in the optimization of efficiency in FEL amplifiers.

Online content

Any methods, additional references, Nature Research reporting summaries, source data, extended data, supplementary information, acknowledgements, peer review information; details of author contributions and competing interests; and statements of data and code availability are available at https://doi.org/10.1038/s41566-022-00995-z.

Received: 29 October 2021; Accepted: 21 March 2022;
Published online: 12 May 2022

References

1. Dhillon, S. et al. The 2017 terahertz science and technology roadmap. *J. Phys. D Appl. Phys.* **50**, 043001 (2017).
2. Lee, Y.-S. *Principles of Terahertz Science and Technology* Vol. 170 (Springer, 2009).
3. Salén, P. et al. Matter manipulation with extreme terahertz light: progress in the enabling THz technology. *Phys. Rep.* **836**, 1–74 (2019).
4. Nanni, E. A. et al. Terahertz-driven linear electron acceleration. *Nat. Commun.* **6**, 8486 (2015).
5. Thumm, M. High power gyro-devices for plasma heating and other applications. *Int. J. Infrared Millim. Waves* **26**, 483–503 (2005).
6. Kemp, M. C. et al. in *Terahertz for Military and Security Applications* Vol. 5070 (eds Hwu, R. J. & Woolard, D. L.) 44–52 (SPIE, 2003).
7. Müller, A.-S. & Schwarz, M. in *Synchrotron Light Sources and Free-Electron Lasers: Accelerator Physics, Instrumentation and Science Applications* (eds Jaeschke, E. J., Khan, S., Schneider, J. R. & Hastings, J. B.) 83–117 (Springer, 2020).
8. Gallerano, G. P. et al. Overview of terahertz radiation sources. In *Proc. 2004 FEL Conference* (eds Bakker, R., Giannessi, L., Marsi, M. & Walker, R.) Vol. 1, 216–221 (JACoW, 2004).
9. Booske, J. H. et al. Vacuum electronic high power terahertz sources. *IEEE Trans. Terahertz Sci. Technol.* **1**, 54–75 (2011).
10. Thumm, M. *State-of-the-Art of High Power Gyro-Devices and Free Electron Masers. Update 2017*, KIT Scientific Report No. 7750 (KIT Scientific Publishing, 2018).
11. Kumar, N., Singh, U., Singh, T. & Sinha, A. A review on the applications of high power, high frequency microwave source: gyrotron. *J. Fusion Energy* **30**, 257–276 (2011).
12. Elias, L. Free-electron laser research at the University of California, Santa Barbara. *IEEE J. Quantum Electron.* **23**, 1470–1475 (1987).
13. Ramian, G. The new UCSB free-electron lasers. *Nucl. Instrum. Methods Phys. Res. A* **318**, 225–229 (1992).
14. Oepts, D., Van der Meer, A. & Van Amersfoort, P. The free-electron-laser user facility Felix. *Infrared Phys. Technol.* **36**, 297–308 (1995).
15. Gallerano, G., Doria, A., Giovenale, E. & Renieri, A. Compact free electron lasers: from Cerenkov to waveguide free electron lasers. *Infrared Phys. Technol.* **40**, 161–174 (1999).
16. Jeong, Y. U. et al. First lasing of the KAERI compact far-infrared free-electron laser driven by a magnetron-based microtron. *Nuclear Instrum. Methods Phys. Res. A* **475**, 47–50 (2001).
17. Knyazev, B., Kulipanov, G. & Vinokurov, N. Novosibirsk terahertz free electron laser: instrumentation development and experimental achievements. *Meas. Sci. Technol.* **21**, 054017 (2010).
18. Gensch, M. et al. THz facility at Elbe: a versatile test facility for electron bunch diagnostics on quasi-CW electron beams. In *Proc. 5th International Particle Accelerator Conference* IPAC14 (JACoW, 2014); https://doi.org/10.18429/JACoW-IPAC2014-TUZA02

19. Shu, X. et al. First lasing of CAEP THz FEL facility. In *Proc. 2017 42nd International Conference on Infrared, Millimeter and Terahertz Waves (IRMMW-THz)* 1–2 (IEEE, 2017).
20. Li, H.-T., Jia, Q.-K., Zhang, S.-C., Wang, L. & Yang, Y.-L. Design of FELiChEM, the first infrared free-electron laser user facility in China. *Chin. Phys. C* **41**, 018102 (2017).
21. Romaniuk, R. S. POLFEL-free electron laser in Poland. *Phot. Lett. Poland* **1**, 103–105 (2009).
22. Nause, A. et al. 6-MeV novel hybrid (standing wave-traveling wave) photo-cathode electron gun for a THz superradiant FEL. *Nucl. Instrum. Methods Phys. Res. A* **1010**, 165547 (2021).
23. Boonpornprasert, P. et al. Start-to-end simulations for IR/THz undulator radiation at PITZ. In *Proc. FEL* (eds Chrin, J., Reiche, S. & Schaa, V. R. W.) 153–158 (CERN, 2014).
24. Musumeci, P. et al. Advances in bright electron sources. *Nucl. Instrum. Methods Phys. Res. A* **907**, 209–220 (2018).
25. Curry, E., Fabbri, S., Maxson, J., Musumeci, P. & Gover, A. Meter-scale terahertz-driven acceleration of a relativistic beam. *Phys. Rev. Lett.* **120**, 094801 (2018).
26. Snively, E., Xiong, J., Musumeci, P. & Gover, A. Broadband THz amplification and superradiant spontaneous emission in a guided FEL. *Opt. Express* **27**, 20221–20230 (2019).
27. Bartolini, R., Doria, A., Gallerano, G. & Renieri, A. Theoretical and experimental aspects of a waveguide FEL. *Nucl. Instrum. Methods Phys. Res. A* **304**, 417–420 (1991).
28. Curry, E., Fabbri, S., Musumeci, P. & Gover, A. THz-driven zero-slippage IFEL scheme for phase space manipulation. *New J. Phys.* **18**, 113045 (2016).
29. Savilov, A. V. Stimulated wave scattering in the Smith-Purcell FEL. *IEEE Trans. Plasma Sci.* **29**, 820–823 (2001).
30. Gover, A. et al. Superradiant and stimulated-superradiant emission of bunched electron beams. *Rev. Mod. Phys.* **91**, 035003 (2019).
31. Duris, J., Murokh, A. & Musumeci, P. Tapering enhanced stimulated superradiant amplification. *New J. Phys.* **17**, 063036 (2015).
32. Sudar, N. et al. High efficiency energy extraction from a relativistic electron beam in a strongly tapered undulator. *Phys. Rev. Lett.* **117**, 174801 (2016).
33. Maxson, J. et al. Direct measurement of sub-10-fs relativistic electron beams with ultralow emittance. *Phys. Rev. Lett.* **118**, 154802 (2017).
34. Alesini, D. et al. New technology based on clamping for high gradient radio frequency photogun. *Phys. Rev. Special Top. Accel. Beams* **18**, 092001 (2015).
35. Calvi, M., Camenzuli, C., Ganter, R., Sammut, N. & Schmidt, T. Magnetic assessment and modelling of the Aramis undulator beamline. *J. Synchrotron Radiat.* **25**, 686–705 (2018).
36. Warren, R. Limitations on the use of the pulsed-wire field measuring technique. *Nucl. Instrum. Methods Phys. Res. A* **272**, 257–263 (1988).
37. Zangwill, A. *Modern Electrodynamics* (Cambridge Univ. Press, 2013).
38. Fisher, A., Musumeci, P. & Van der Geer, S. Self-consistent numerical approach to track particles in free electron laser interaction with electromagnetic field modes. *Phys. Rev. Accel. Beams* **23**, 110702 (2020).
39. Giannessi, L., Musumeci, P. & Quattromini, M. TREDI: fully 3D beam dynamics simulation of RF guns, bendings and FELs. *Nucl. Instrum. Methods Phys. Res. At* **436**, 443–444 (1999).
40. Doria, A., Gallerano, G. P., Giovenale, E., Messina, G. & Spassovsky, I. Enhanced coherent emission of terahertz radiation by energy-phase correlation in a bunched electron beam. *Phys. Rev. Lett.* **93**, 264801 (2004).
41. Sun, Y.-E. et al. Tunable subpicosecond electron-bunch-train generation using a transverse-to-longitudinal phase-space exchange technique. *Phys. Rev. Lett.* **105**, 234801 (2010).
42. Musumeci, P., Li, R. & Marinelli, A. Nonlinear longitudinal space charge oscillations in relativistic electron beams. *Phys. Rev. Lett.* **106**, 184801 (2011).
43. Muggli, P., Yakimenko, V., Babzien, M., Kallos, E. & Kusche, K. Generation of trains of electron microbunches with adjustable subpicosecond spacing. *Phys. Rev. Lett.* **101**, 054801 (2008).
44. Boscolo, M., Ferrario, M., Boscolo, I., Castelli, F. & Cialdi, S. Generation of short THz bunch trains in a RF photoinjector. *Nucl. Instrum. Methods Phys. Res. A* **577**, 409–416 (2007).
45. Zen, H., Ohgaki, H. & Hajima, R. Record high extraction efficiency of free electron laser oscillator. *Appl. Phys. Express* **13**, 102007 (2020).
46. Orzechowski, T. et al. High-efficiency extraction of microwave radiation from a tapered-wiggler free-electron laser. *Phys. Rev. Lett.* **57**, 2172–2175 (1986).

Methods

Pegasus beamline set-up. The drive for the photoinjector is a frequency-tripled Ti:sapphire laser system, which provides to the cathode 266-nm pulses of 100-μJ energy with an r.m.s. spot size of ~0.9 mm and FWHM pulse length of 100 fs. A 1.6-cell S-band RF gun accelerates the electrons to 3.6 MeV of total energy before injection into an 11-cell S-band high-shunt-impedance linac with peak gradient of 20 MV m^{-1}. The linac centre is at a distance of 1.7 m from the cathode. To vary the injection energy into the FEL, the linac phase is tuned 50–75° off crest to compress the electron bunch length at the undulator entrance located 4.6 m from the cathode. The transverse spot size at the undulator entrance is controlled using a gun solenoid and a quadrupole triplet. Three magnetic spectrometers are installed on the beamline, one before the undulator (spectrometer 1) and two, the high-resolution spectrometer 2 and low-resolution spectrometer 3, after the undulator.

Theseus undulator. The tapered helical undulator is based on a double Halbach array of permanent magnets, rotated and shifted by 90° with respect to each other. The undulator is composed of 28 full periods with period length of 32 mm, as well as an entrance and exit section, for a total length of 0.96 m. The gap at the undulator entrance is 7 mm. The tapered undulator magnetic field profile is optimized through simulations and measured and tuned using Hall-probe and pulse-wire scans. After 50 mm, the gap is adjusted to taper the on-axis field quadratically from 0.73 T to 0.52 T. The vacuum pipe has an outer diameter of 5.56 mm and inner diameter of 4.54 mm. The undulator is aligned by centring the entrance and exit flanges on the reference alignment green laser injected on the electron-beam axis using a retractable mirror immediately after the gun. The undulator supports allow for fine adjustment of its position and angle. Two pairs of steering magnets before and after the undulator are used to optimize the transmission of the beam through the system.

Electron-beam diagnostics. The energy spectrum of the electron beam is measured before the undulator using spectrometer 1 (radius of curvature of 0.67 m, bending angle of 45°), and after the undulator by spectrometer 2 and spectrometer 3. Spectrometer 2 is a round-pole dipole that bends the beam by 45° with a radius of curvature of 0.093 m. The spectrometer screen is located 0.15 m downstream of the dipole. The measured dispersion at the screen is in agreement with the calculated value of 0.13 m. Given a camera calibration of 41 μm per pixel, each pixel corresponds to 3×10^{-4} relative energy variation. The 12-mm opening of the vacuum pipe at the exit of the spectrometer limits the acceptance of this diagnostic screen to ±9%. When the interaction is tuned close to the zero-slippage condition, some particles lose more than 20% of their energy (while others gain up to 5%), so full energy spectra can only be obtained by stitching images recorded at different dipole currents. An additional spectrometer (spectrometer 3) using a short rectangular dipole providing very small dispersion is used on the straight-through beamline for independent confirmation of the average beam energy loss, validating the stitching approach. A 9.6-GHz deflector with a maximum deflecting voltage of 500 kV is used to streak the beam vertically and record the longitudinal phase space image shown in Fig. 2c. The charge is measured by a turbo integrating current transformer located 1 m from the cathode. Each fluorescent screen on the beamline is calibrated using a Faraday cup to allow charge measurements by integrating the electron-beam signal, facilitating transmission loss measurements along the beamline. Charge and energy shot-to-shot fluctuations over a typical dataset (for example, a high-resolution interferometry scan) are measured to be 5% and <0.5%, respectively. The r.m.s. pointing stability of the electron beam on the screen just before the undulator is measured at 12% of the electron-beam r.m.s. spot size.

Simulation methods. Standard FEL codes typically neglect radiation dispersion in a waveguide and use simplified models for space charge effects. To accurately model the experiment, we utilized the newly developed GPT FEL module[38], which calculates the FEL interaction of high-brightness electron beams in a magnetic undulator using a frequency and modal expansion of the electromagnetic field, evolving each mode using energy conservation. The advantage of using a GPT extension is that it can naturally include space charge and beamline field maps for a seamless start-to-end simulation. The GPT FEL simulation tracks 10,000 particles with an electromagnetic field modelled using $N=92$ different frequency modes, equally spaced and covering the region from 80 to 660 GHz. Addition of the next three higher-order spatial modes of the waveguide did not affect the results. The power attenuation coefficient of the stainless-steel waveguide ranges from $\beta=3.47$ dB m^{-1} at 100 GHz to $\beta=5.2$ dB m^{-1} at 500 GHz. Simulations led to the realization that the effective undulator K parameter for electrons wiggling off-axis is larger (2% larger in our design), mainly due to the addition of a radial force from the non-zero B_z field component. Importantly, the results contained in this Article provide the first benchmarking of the GPT FEL extension module with experimental results, validating this approach for the study of the interaction of the relativistic beam with the electromagnetic modes of the circular waveguide in the presence of both space charge and dispersion effects.

Terahertz transport. A 4.7-mm-diameter short extension pipe is used to collect the radiation at the exit of the undulator and couple to free space. An OAP mirror (gold-plated, with a 5-mm-diameter hole and focal length of 76.2 mm) is installed after the undulator to collimate and reflect the terahertz radiation at 90° out of the vacuum system through a z-cut quartz terahertz window. The total energy in the radiation pulse is measured by placing a removable 50-mm-diameter OAP mirror immediately outside the terahertz vacuum window to focus the radiation onto a 9-mm-diameter pyroelectric Gentec terahertz detector. The detector was factory-calibrated at a 1-mm wavelength to 7 nJ mV^{-1}. The transmission of the terahertz transport system from the undulator to the detector is measured by using a 10-mW continuous-wave 140-GHz radiation source placed at the entrance of the undulator. It was found that 27% of the radiation at the undulator exit is then collected at the detector. The main reason for the poor transmission are losses on the collecting pipe, the in-vacuum apertures, the 5-mm hole in the OAP and the vacuum window.

Terahertz interferometry. When the last OAP is removed, the collimated terahertz radiation can be redirected to a Michelson interferometer. A lossy (30%) beamsplitter separates the radiation along two paths. After reflecting off mirrors, the beams recombine and are focused onto a pyroelectric detector that can record the field autocorrelation of the radiation pulse when the interferometer path length difference is adjusted remotely. The signal on the interferometer is less than 10% of the reference signal due to the large absorption of the beamsplitter and additional diffraction losses caused by the relatively small-aperture (40-mm-diameter) terahertz window.

Data availability

The datasets for the beam energy spectrum as a function of charge and the interferometry scans at different beam energies are available from the corresponding author upon reasonable request.

Code availability

The GPT input file for simulating the entire Pegasus beamline, including the gun, the RF buncher linac and the interaction with the TE11 mode in the undulator, is available from the corresponding author upon reasonable request.

Acknowledgements

This work was supported by NSF grant no. PHY-1734215 and DOE grants nos. DE-SC0009914 and DE-SC0021190. The undulator construction was carried out under SBIR/STTR DE-SC0017102 and DE-SC0018559.

Author contributions

A.F. and Y.P. carried out the measurements and analysed the data. M.L. and A.O. helped with UCLA Pegasus beamline operation, including alignment, vacuum and controls. P.M. proposed and supervised the experiment. A.M. participated in the TESSA development and is the principal investigator on one of the supporting grants. R.A. and T.H. were responsible for the undulator construction. A.F., Y.P. and P.M. prepared the manuscript, which was revised and edited by all co-authors.

Competing interests

The authors declare no competing interests.

Additional information

Correspondence and requests for materials should be addressed to A. Fisher, Y. Park or P. Musumeci.

Peer review information *Nature Photonics* thanks Lixin Yan and the other, anonymous, reviewer(s) for their contribution to the peer review of this work.